Fracture, Fluid and Saturation Effects on the Seismic Attributes of Hydrothermally Altered Rocks from Southern Negros Geothermal Field, Philippines

David Carlo Austria[1,2] and Philip M. Benson[1]

[1] Rock Mechanics Laboratory, School of Earth and Environmental sciences, University of Portsmouth, PO1 3QL, U.K.

[2] Geosciences and Reservoir Engineering Group, Energy Development Corporation, Ortigas Centre, Pasig City, Philippines

Corresponding authors: David Carlo Austria (austria.ds@energy.com.ph), Philip M. Benson (philip.benson@port.ac.uk)

Key words: geothermal, acoustic emission, seismic attributes, triaxial vessel

Highlights:

- Shear fracture development during triaxial deformation may be controlled by cutting notches to force formation of a natural fracture surface which can be accessed by miniature boreholes for fluid flow
- Elastic wave velocities and dynamic elastic parameters can be used to infer the state of material fracturing
- Acoustic emission occurs with rapid pore fluid venting under conditions similar to geothermal environments
- Extraction of fluids in a geothermal environment has a significant effect on seismicity

Abstract

Seismic based geophysical methods are seeing increased usage in evaluating geothermal resources in order to maximize resource potential. However, interpreting geophysical data (such as velocities and dynamic modulus and fracture density/alignment) generated from geothermal reservoirs remains difficult. Here we present the results of a new laboratory study measuring seismic attributes of fresh and hydrothermally altered rocks from a Philippine geothermal field (Southern Negros Geothermal Project - SNGP) during triaxial deformation. Two types of rocks were obtained by sub-coring samples of low porosity (~1%) andesite and higher porosity (~10%) volcaniclastic samples from the SNGP. Samples were prepared with two offset drill holes to allow a natural fracture to permit fluid flow along the fracture. An embedded array of Acoustic Emission (AE) sensors allows elastic wave and induced microseismic data to be collected. We measure a significant reduction in elastic wave velocities and moduli, with the exception of Poisson's ratio, after shear fracture development. An initially pre-fractured permeability of approximately 10^{-17} m^2 is measured. We find that the permeability decreases from 2.0 $x10^{-14}$ m^2 to lower than 7.4 $x10^{-15}$ m^2 as the confining pressure is increased from 5 MPa to 30 MPa. A concomitant increase in P and S-wave velocities, dynamic bulk and Young's moduli are also measured. Finally, we simulate a geothermal 'venting' situation by intentionally releasing the high pore fluid (water) pressure from 10-50 MPa to ambient pressure, generating a swarm of AE that increases in duration with higher pore pressure. We postulate that this is due to fluid phase change (liquid to gas) and movement along the natural fracture plane and damage zone.

1. Introduction

Inferring rock properties from geophysical data has been the subject of numerous studies for the purpose of exploring and developing energy resources (e.g. Batzle and Wang, 1992; Siratovich et al., 2014; Dupuy et al., 2015; Bonner et al., 2015). A key goal is to gain insight on the links between measurements that are hard or time-consuming to obtain (such as permeability) and geophysical data such as seismic wave velocity. However, although there is an extensive literature for petrophysical properties in reservoirs related to the hydrocarbon industry, there are fewer studies in the case of geothermal rock physics (e.g. Geraud et al., 2010; Siratovich et al., 2016; Kushnir et al., 2018). This is becoming increasingly important as the

use of seismic attributes are now frequently being used to 'image' geothermal fields. A number of laboratory experiments have been reported, such as on samples taken from the reservoir rock of the Geysers geothermal field (e.g. Boinott et al., 1995). These data show the effects of both saturation and fracturing on the P-wave and S-wave elastic velocity, as well as the Vp/Vs ratio, a very common petrophysics parameter. And, whilst this data is valuable for interpreting seismic data for geothermal exploration and development, it is also clear that additional, site-specific, rock physics studies are needed (e.g. Siratovich et al., 2014). To this end, a number of studies have been reported that seek to measure and link key rock properties and then relate this to changes in observable seismic data. This is becoming especially important as seismic imaging techniques continue to improve and open new avenues in subsurface imaging (e.g. Julian et al., 2010; Julian and Foulger, 2010; De Siena et al., 2014; Hutchings et al., 2015).

A key tool in making new links to field data is laboratory rock physics, which allows a range of subsurface processes to be simulated under controlled conditions (e.g. Lockner et al., 1991; Ayling et al., 1995; Benson et al., 2007; Faulkner et al., 2017; Browning et al., 2016). Recent work has shown that seismic attributes of different rock types (elastic velocities and moduli) may be determined during deformation at elevated pressure and temperature (e.g. Ayling et al., 1995; Blake and Faulkner, 2015; Harnett et al., 2018; Blake and Faulkner, 2020). The initial stage of triaxial rock deformation is typically marked by increasing differential stress acting on the sample, closing micro-and macro scale cracks. This results in increasing elastic wave velocities and other attributes (Ayling et al., 1995; Harnett et al., 2018). Additional stress initiates inelastic deformation and crack formation, leading to overall decrease in seismic attributes (Ayling et al., 1995) as cracks nucleate and connect, generating acoustic emission (the laboratory analogue to tectonic earthquakes) and modifying material stiffness (Young's modulus) and Poisson's ratio. However, even though the results from these previous studies have shown the importance of seismic data on inferring rock properties, more data is needed, and in particular under geothermal conditions and using rocks from geothermal reservoirs, in order to better match geophysical data to conditions at depth.

Here we report a set of laboratory experiments from borehole samples of andesite and volcaniclastic rocks from the Southern Negros Geothermal Project. We compare elastic wave velocity and dynamic moduli to fluid flow along a freshly-generated shear fracture connecting

fluid injection/drain ports, and with respect to initial sample porosity and post-test fracture damage. In addition, while it is important to measure seismic attributes such as P and S wave velocities, it is also important to understand the contribution of geothermal exploitation and development to seismicity. Acoustic Emission (AE) are a proven excellent analogue to field data (e.g. Lockner et al., 1991; Benson et al., 2007; Fazio et al., 2017), and can help relate field seismic methods in terms of their links to material properties (e.g. Vinciguerra et al., 2005). Using these methods, we compare and contrast the improved permeability of fractured volcanic rocks with increasing burial depth, and explore the effects of the changing magnitude of fluid flow through the fractured sample to the concomitant change in seismic attributes.

2.0. Material, Equipment and Methods

2.1. Sample description and preparation

The Southern Negros Geothermal Project (SNGP) is a high temperature, liquid dominated system situated at the western section of central Philippines (Rae et al., 2004) where magmatism is associated with the east dipping Negros Trench. This type of geothermal system has temperatures of above 225ºC and occurs in active margins (Hochstein, 1990). The SNGP has two production sectors where extractions of high temperature fluids are carried out. These production sectors are found south of the Okoy River and north-west of the prominent volcanic peaks in the area, Mt. Talines and Cuernos de Negros (Figure 1). While production activities are concentrated at the south, fluid reinjection is conducted on the northern section of the field along the Okoy River which is controlled by the ENE-WSW trending Puhagan Fault zone (Pastoriza et al., 2018). The division of SNGP into two sectors is due to variation in reservoir pressure, injection returns and over all development strategy, with sector 1 being developed a decade earlier than sector 2 (Malate et al., 2008).

The routine drilling activities at the SNGP have allowed direct access to subsurface rock units, from which a number of sub-cores were taken in order to examine seismic attributes with changing pressure conditions. This provides a valuable set of advantages in the sense that these samples are retrieved from depth, with relatively few studies having reported data using rocks taken directly from a geothermal reservoir (e.g. Geraud et al., 2010; Kushnir et al., 2018). Two sample types were utilized in this study. Firstly, a volcaniclastic rock (SNV) described as having

126 a very fine-grained matrix and clasts consisting of angular to sub angular lithic fragments and
127 plagioclase and amphibole minerals that are identifiable under the petrographic microscope.
128 Devitrification process appears to have occurred in SNV samples, replacing volcanic glasses
129 by zeolites occurring as radial fans in amygdales. The lithic fragments are found to consist of
130 porphyritic andesite and volcaniclastic rocks. SNV is marked by presence of significant void
131 spaces and fragmented texture. The second type of sample is a porphyritic andesite (SNA) that
132 exhibits fractures filled with silica/quartz. SNA samples consist mainly of pyroxene and
133 plagioclase phenocrysts wherein some of the plagioclase crystals were partially replaced by
134 hydrous minerals such as kaolinite and are partially embayed. Both types of sample belong to
135 the Southern Negros Formation which is described as a sequence of polymictic volcaniclastic
136 breccia and coherent volcanic rocks (Rae et al., 2004). The Southern Negros Formation is found
137 to exhibit alteration assemblage from low-temperature illite alteration, consisting mainly of
138 illite and or smectite, to high-temperature propylitic alteration near the upflow zone, composed
139 mainly of secondary mineral epidote (Rae et al., 2003).
140
141 Aside from rock type (composition and texture), SNV and SNA exhibit significant
142 differences in porosity and density which were acquired with the use of hydrostatic weighing
143 and helium pycnometer on a number of disc samples cut from the cylindrical samples subjected
144 to the tri-axial experiment. SNV samples have porosities ranging from 10 to 13% and bulk
145 densities of 2.3 to 2.4 g/cm^3. Conversely, SNA samples have lower porosity of <1% and higher
146 bulk density of 2.7 g/cm^3. The sample properties are tabulated in Table 1.
147
148

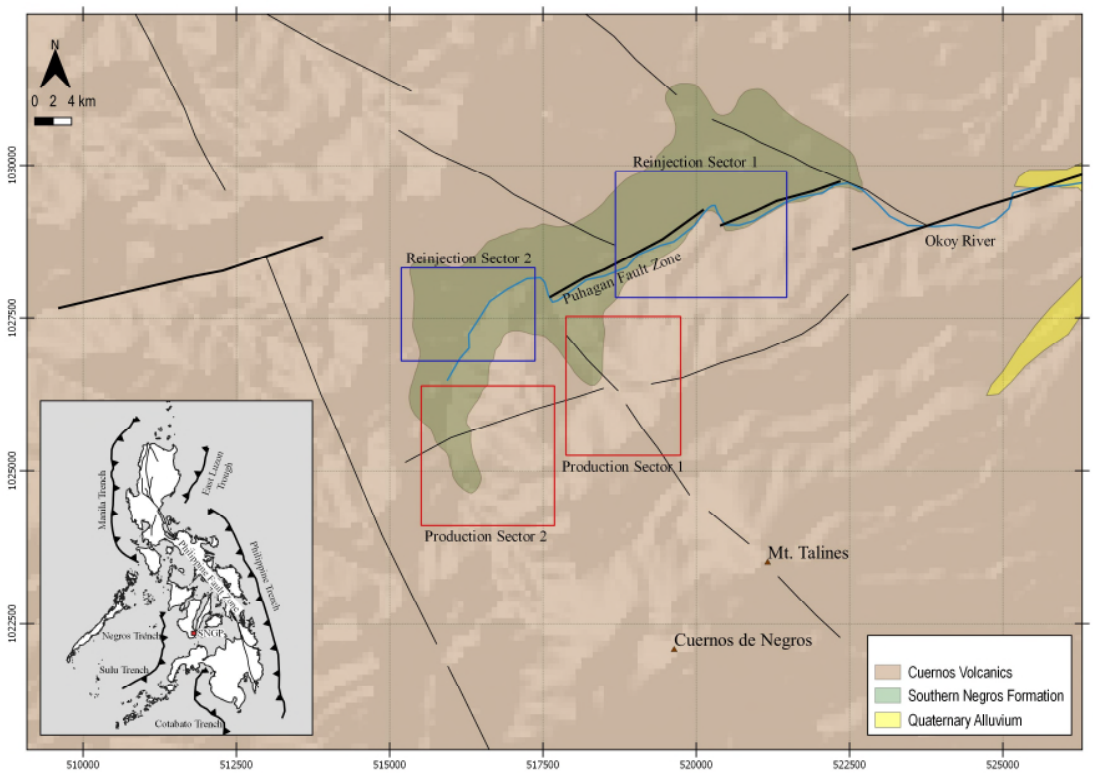

Figure 1. Simplified geologic map of the Southern Negros Geothermal Field showing the production (red rectangles) and reinjection (blue rectangles) sectors (modified after Pastoriza et al., 2018; Rae et al., 2003). Also shown are the key lineaments (black lines) identified by Pastoriza et al., (2018) and the Okoy River (light blue line). The tectonic map of the Philippines (inset) shows the location of the SNGP with respect to major geologic structures in the area (modified after Aurelio et al., 2013). SRTM data taken from Jarvis et al., (2008).

Table 1. Porosity, density and sample type of SNGP samples.

Sample Type	Sample Name	Porosity (%)	Density (g/cm^3)	Rock Type
AA4 (SNA)	AA4-1	0.1	2.7	Porphyritic Andesite
	AA4-2	0.1	2.7	
	AA4-3	0.1	2.7	
	AA4-4	0.1	2.7	
AA3	AA3-1	0.6	2.68	Porphyrictic andesite
	AA3-2	0.6	2.68	
AA1	AA1-1	5.7	2.55	Porphyrictic andesite
	AA1-2	5.7	2.55	
	AA1-3	5.7	2.55	
AA5	AA5-1	10.6	2.42	Highly Altered volcaniclastic rock
AA6 (SNV)	AA6-1	12.6	2.32	Volcaniclastic rock
	AA6-2	12.6	2.32	
	AA6-3	12.6	2.32	

Cylindrical core samples of 100mm long and 40mm diameter were prepared using a hollow diamond core drill and diamond-grinding wheel to ensure sample ends were flat and parallel to within 0.01mm. An important aspect of the project is to study the evolution of fracture permeability along a natural fracture plane (damage zone) resulting from the application of a principal stress. This has the advantage of being more representative of the types of undulating surfaces seen in nature, compared to pre-cut plane often utilized by previous studies (e.g. McLaskey and Lockner, 2014; Faulkner et al., 2017; Passelègue et al., 2016). The disadvantage of this, however, is the more difficult preparation and ensuring the fluid flows along the developed shear plane. To achieve this, two offsets notches were cut across the diameter of the sample at the side on both ends (Figure 2) to promote a connecting 30° shear fracture. This natural fracture was accessed by drilled holes at both ends of the sample to intersect the shear plane (Figure 2).

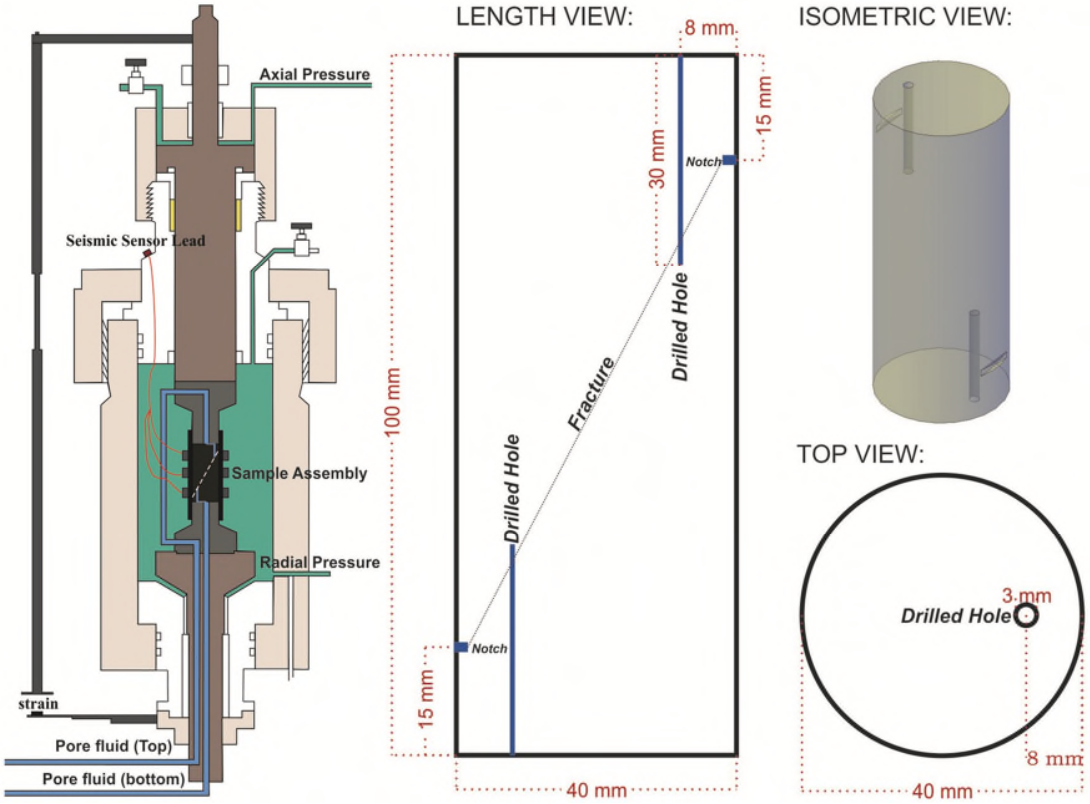

Figure 2. Schematics of the triaxial deformation equipment utilized for the study (modified after Benson et al., 2019) and drill core setup using pre-cut notches and boreholes to promote formation of a natural fracture and damage zone connecting the drilled hole for fluid flow measurement along the failure plane.

2.2. Shear fracture development

A conventional triaxial vessel (Sanchez Technologies) was used to fracture the samples. This consists of a 100 MPa pressure chamber fitted with an electronically compensated servo-controlled axial piston capable of providing 680 MPa principal stress using a sample diameter of 40mm (Figure 2). Confining and axial pressures are regulated by precision piston pumps using high-flash point oil as pressurising medium. The vessel is additionally fitted with two servo-controlled precision pumps to independently introduce a (fixed) pore fluid pressure to each end of the rock specimen, providing upstream and downstream fluids pressures and concomitant fluid volume change. Samples are encapsulated in an engineered rubber (Nitrile) jacket fitted with 18 ports for acoustic emission (AE) and other sensors, and to separate the water-saturated sample from the confining oil. The AE sensors are custom-built miniature AE sensors consisting of an aluminium casing fitted with a waveguide, a 3.5 mm thick Lead-Zirconate-Titanate (PZT) piezoelectric ceramic with 1 MHz resonant frequency, and backed with a short tungsten rod to reduce waveform resonance (Fazio et al., 2017). The sensors convert incoming mechanical signals to voltages that are then amplified by between 30 to 70 dB before being fed into two independent AE recorders for analysis. Axial strain data from the sample were acquired using an Eddy Displacement System. This is an external non-contact transducer system attached to a stationary ring assembly at the bottom of the tri-axial vessel which measures the distance to three steel targets attached to the (moving) top piston ring to measure average displacement. Radial strain is acquired through the use of internal Linear Variable Differential Transformer directly mounted on a cantilever attached to the rock sample via 4 jacket ports (Gehne et al., 2019).

Two types of experiments are performed (Figure 3). Firstly (Fig. 3A), a triaxial deformation experiment is conducted ($\sigma_1>\sigma_2=\sigma_3$) at elevated confining pressure (Pc) to generate a shear fracture plane, followed by lowering of differential stress to re-establish isostatic conditions ($\sigma_1=\sigma_2=\sigma_3$). Once achieved, the effective pressure (Pp-Pc) is increased stepwise with water flow rate across the drilled injector/receiver ports and elastic wave velocity measured at each step. This is repeated with stepwise decreasing effective pressure. Secondly (Fig. 3B), the same type of deformation experiment is performed. Then, once a target pore fluid pressure is reached, the vessel and assembly is heated to a target temperature of 175 °C. A fast-acting valve is then

activated to vent the elevated pore pressure (water) to promote phase change (water to steam) and thus to record the effect of fluid pressure release and fluid-mechanical effects (from liquid to a steam/gas mixture) on the recorded fluid-pressure and AE, which are recorded at the same high sampling rates to ensure no information is lost and to ensure no timing errors between the pore fluid pressure (venting data) and the AE data recorders.

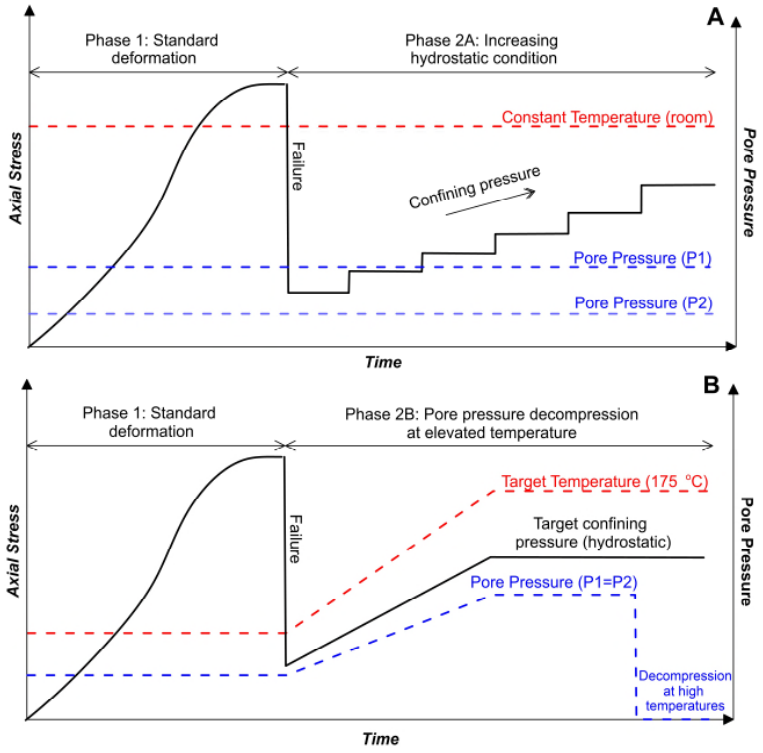

Figure 3. Schematic axial stress–time plots showing the two types of experiments conducted for this study. Panel (A) shows the post-failure stepwise increase in confining pressure under hydrostatic conditions where data is acquired at each step. Panel (B) shows the same initial fracture development followed by the procedure for pore pressure decompression at high temperature conditions.

Table 2. Sample dimensions and parameters used during deformation

Sample Type	Dimension (mm)	Parameters during deformation

	Sample Name	(height x diameter)	Pore fluid pressure (MPa) (P2 and P1)	Confining Pressure (MPa)	Strain rate (s^{-1})
AA4 (SNA)	AA4-1	100.29 x 40.15	0.8 and 1.3	6.1	3 x 10^{-6}
	AA4-2	100.31 x 40.13	0.8 and 1.3	6.1	3 x 10^{-6}
	AA4-3	100.45 x 40.15	0.8 and 1.3	6.1	3 x 10^{-6}
	AA4-4	100.61 x 40.14	0.8 and 1.3	6.1	3 x 10^{-6}
AA3	AA3-1	100.07 x 40.14	0.8 and 1.3	6.1	3 x 10^{-6}
	AA3-2	100.47 x 40.16	0.8 and 1.3	6.1	3 x 10^{-6}
AA1	AA1-1	100.68 x 40.15	0.8 and 1.3	6.1	3 x 10^{-6}
	AA1-2	100.33 x 40.17	0.8 and 1.3	6.1	3 x 10^{-6}
	AA1-3	100.09 x 40.14	0.8 and 1.3	6.1	3 x 10^{-6}
AA5	AA5-1	100.04 x 40.15	0.8 and 1.3	6.1	3 x 10^{-6}
AA6 (SNV)	AA6-1	100.16 x 40.13	0.8 and 1.3	6.1	3 x 10^{-6}
	AA6-2	100.32 x 40.15	0.8 and 1.3	6.1	3 x 10^{-6}
	AA6-3	100.03 x 40.17	0.8 and 1.3	6.1	3 x 10^{-6}

2.3. Fluid flow & permeability

During phase (2A) of the experiment as shown above, the steady-state flow method is used to calculate an 'effective' permeability (e.g. Gehne and Benson, 2018) along the fracture damage zone. The fluid flow rate is directly known from the change in pump volume with time, which is measured stepwise with increasing confining pressure simulating burial depth. At each effective pressure steady state flow is then ensured by allocating a minimum of 10 minutes. This allows time for fluids to be expelled or imbibed by void spaces, and re-establishes a steady flow condition through the fractured sample with upstream and downstream pressure pumps exhibiting similar but opposite flow rate values (acting as a check for leaks in the system). The resulting flow rate from the pressure pumps were then averaged and input into Darcy's equation to calculate and model the permeability of the fractured zone:

$$k = \frac{Q\ L\ \eta}{(WH)\ (P - P')} \qquad \text{Eqn. (1)}$$

where: k is effective permeability (m^2)
Q is volumetric flow rate (m^3/s)
L is length of the fracture zone (m)
η is the fluid viscosity at room temperature (8.9x10^{-4} Pa.s)
W is the width of the fracture zone (m)

H is the thickness of the fracture zone (m)
P is the entry pore pressure (Pa)
P' is the exit pore pressure (Pa)

Unlike when considering fluid flow in an entire porous cylinder (conduit or pipe) here we apply Darcy's equation to a fracture zone which we take as a rectangular prism with known dimensions. The length and width are set following the dimension of the notches, while the height (or thickness of the fracture zone) is modelled at different values ranging from 1 to 10 mm. These result in a range of 'effective' permeability in the deformed sample at each confining pressure. Other parameters are recorded directly by the instrument including the fluid pressures and volume change with time.

2.4. Acoustic Emission and elastic-wave velocities

Acoustic Emission is generated from natural crack formation and fracture development while the samples are undergoing deformation, and is the laboratory proxy to field scale earthquakes (e.g. Benson et al., 2007). In the setup used here, AE data is recorded continuously on two independent AE recorders that operate simultaneously, taking their input from the same array of 12 AE sensors after pre-amplification of the signal by 30-70 db (selectable). The first system (ITASCA-Image Milne) records a discrete waveform time range across all 12-channels when any single channel exceeds a set threshold voltage of 100mV in a window of 200us. The second system (ITASCA-Image Richter) records all 12 channels regardless if there are AEs or not. This data type is capable of capturing more acoustic emissions as the signal processing is performed after the experiment. Unlike the triggered data, this allows the continuous data to be 'harvested' post-test using more stringent criterion. In this way, the continuous data processing procedure filters out noise and improves the overall quality of harvested events. Both systems operate at 10 MHz and are described in Gehne et al. (2019).

Active surveys for elastic-wave velocity determination are taken by pulsing a high voltage spike through each of the same 12 sensors in sequence, controlled and timed using a dedicated Pulser Interface Unit (PIU) to permit stacking of 32 traces per sensor to improve signal to noise (similar to field reflection seismic acquisition). As each sensor pulses, the remaining 11 sensors receive, allowing signal propagation in different directions (e.g. Harnet et al., 2018). Arrival

285 times of both P and S waves after propagation are recorded on each sensor (of known location)
286 allowing velocity to be calculated using the time-of-flight method (Birch, 1960). The dynamic
287 elastic properties are then derived using the velocity data following the equations below.

288 $$\text{Bulk Modulus (B)} = \rho\,(V_P^2 - \frac{4}{3}V_S^2) \qquad \text{Eqn. (2)}$$

289 $$\text{Young's Modulus (E)} = \frac{\rho V_S^2(3V_P^2 - 4V_S^2)}{V_P^2 - V_S^2} \qquad \text{Eqn. (3)}$$

290 $$\text{Poisson's Ratio } (\sigma) = \frac{V_P^2 - 2V_S^2}{2(V_P^2 - V_S^2)} \qquad \text{Eqn. (4)}$$

291
292 where: Vp is P-wave velocity (km/s)
293 Vs is S-wave velocity (km/s)
ρ is density (g/cm^3)
294
295 **3. Results**
296 **3.1. Elastic wave velocities of SNGP samples**
297 The SNA samples have initial (at an isostatic pressure of 5 MPa) P-wave and S-wave velocities
298 of 5340 m/s and 2430 m/s respectively (Figure 4). As the deformation proceeds (phase 1) the
299 velocities increase until approximately 3500s with the P-wave velocity reaching a maximum of
300 5700 m/s before sample failure at approximately 4000s. The S-wave velocity increases to a
301 maximum of approximately 2500 m/s at 3000s after which velocity starts to decrease (to 2350
302 m/s just prior to sample failure). After failure, axial stress is intentionally lowered to re-establish
303 an isostatic stress state (approximately 4500s) with P-wave and S-wave velocities of 4250 m/s
304 and 1500 m/s respectively. Subsequently, in phase 2A of the experiment, confining pressure is
305 increased stepwise. P-wave velocity increases to 4800 m/s at 6200s (10 MPa confining
306 pressure) followed by a roughly linear increase to 5100 m/s at 12000s (30 MPa). For S-wave
307 data, an approximate linear increase in velocity is measured after failure to 1800 m/s at 12000s
308 (30 MPa). Flow rate decreases exponentially during this time from 7.7 μl/s to 0.3 μl/s.

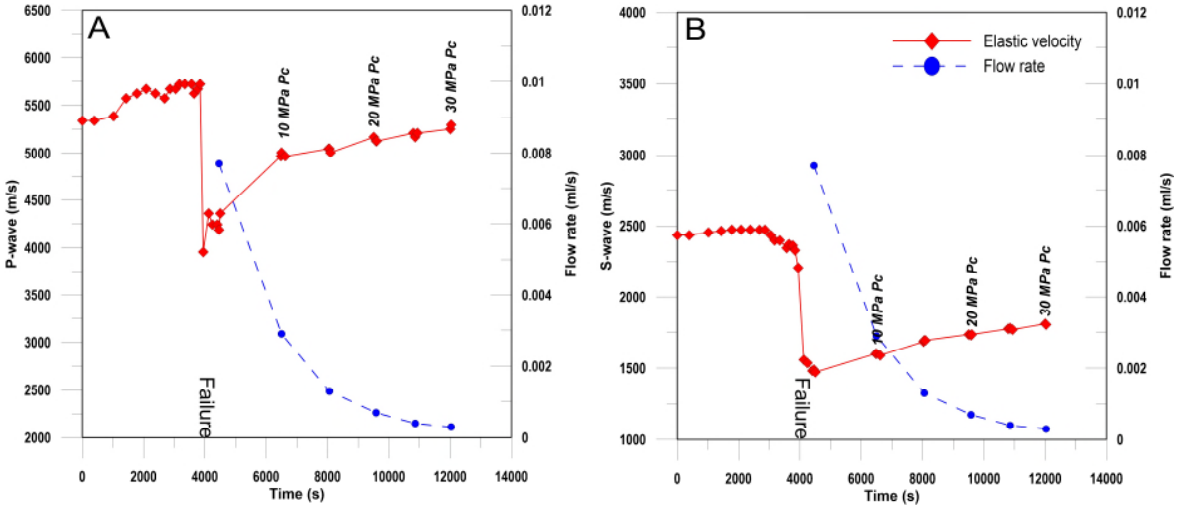

Figure 4. P-wave (panel A) and S-wave (Panel B) elastic velocities (solid lines) in SNA undergoing fracture formation and damage zone development. Flow rate data (dashed lines) acquired after failure is also plotted as a function of stepwise increasing effective pressure (annotated).

Figure 5 uses P-wave and S-wave data to calculate dynamic Poisson's ratio (Fig. 5A), Bulk modulus (Fig. 5B) and Young's modulus (Fig. 5C) during the same time period of deformation and fracture. The resulting initial values are 0.37, 78 GPa and 35 GPa respectively. At the moment of failure, all properties exhibit a significant permanent reduction except for Poisson's ratio which recovers quickly to a value of approximately 0.43, higher than pre-failure modulus. Bulk modulus decreases to 40 GPa whereas the Young's modulus decreases to 15 GPa. Both bulk and Young's modulus then exhibit increasing trends (recovery) as confining pressure is increased stepwise (4000 to 12000s) reaching 75 and 23 GPa respectively at the maximum 30MPa effective pressure. However, neither moduli re-achieve pre-failure levels. Conversely, Poisson's ratio exhibits a decreasing trend as a response to isostatic stress increase after failure, remaining at above 0.41.

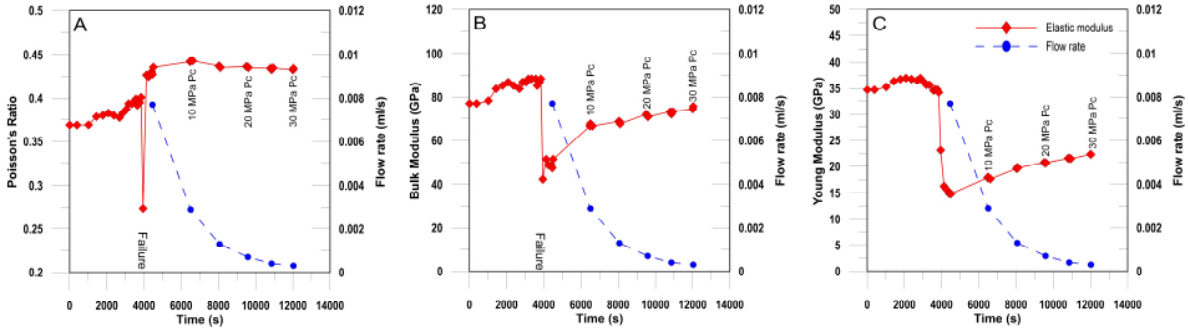

Figure 5. Dynamic modulus evolution (red) in the SNA while undergoing deformation and fracture development. Poisson's ratio (panel A), bulk modulus (panel B) and Young's modulus (panel C) are plotted with flow rate data (blue) acquired after failure (at approximately 4000s) and following increase in confining pressure (Pc).

The low density (<2.45 g/cm^3), high porosity (10-12%) SNV samples exhibit lower elastic wave velocities and seismic attributes. Figure 6 shows the initial P-wave and S-wave velocities of 2500 m/s and 1450 m/s respectively. In common with the SNA data, both velocities increase with time until failure at approximately 1800s, reaching 2800 m/s for P-wave velocity and 1650 m/s for S-wave. However, a few notable differences are also evident compared to the SNA elastic wave velocities. Rather than a sharp decrease, the reduction in elastic wave velocity occurs more gradually, starting from maximum values at approximately 1900s that coincides with peak differential of approximately 60 MPa. P-wave velocity decreases to approximately 2400 m/s while S-wave velocity decreases to 1400 m/s over approximately 600s (failure). After failure at 2500s, differential stress is lowered to achieve isostatic conditions at 5 MPa confining pressure for phase 2A of the experiment. As pressure is increased stepwise to 30 MPa (10800s), P-wave velocity reaches 3000 m/s, higher than its pre-failure peak (Figure 6A) with S-wave increasing to 1500 m/s in an approximately linear fashion. Fluid flow though the fracture decreases during phase 2 from 10.2 µl/s to 5 µl/s.

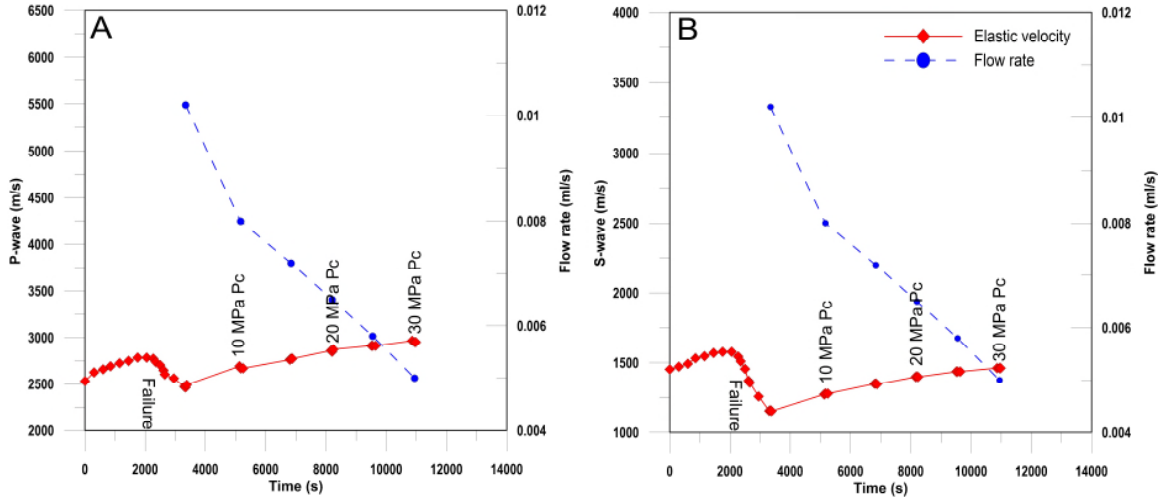

Figure 6. P-wave (Panel A) and S-wave (Panel B) elastic wave velocities showing reduction as a response to crack propagation and fracture development (red) in SNV. Flow rate data (blue) exhibits decreasing trend with increasing confining pressure post failure.

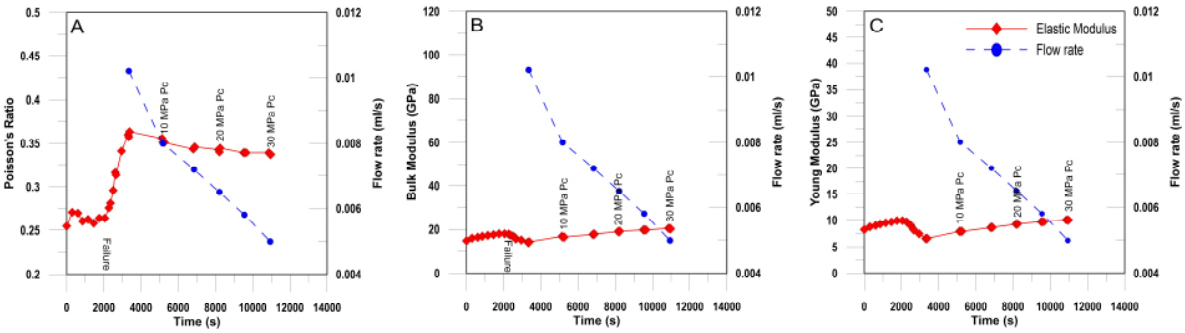

Figure 7. Dynamic moduli of the porous and low density volcaniclastic rock (SNV) while undergoing deformation and fracture development. Flow rate data is plotted in blue. Poisson's ratio (A) showing opposite response to failure compared with bulk modulus (B) and Young's modulus (D).

Using the elastic wave data for SNV (Figure 6) to calculate Poisson's ratio (Fig. 7A), Bulk Modulus (Fig. 7B) and Young's modulus (Fig. 7C) yields initial values of 0.27, 15 GPa and 8 GPa, respectively. The values increase with sample strain (time from 0 to approximately 2000s) with the exception of Poisson's ratio which stays approximately constant (Fig. 7A). At peak differential stress, bulk modulus reaches 18.5 GPa while Young's modulus increases to 10 GPa. The most sensitive parameter to the changing stress state is Bulk modulus, which decreases from 18.5 MPa to approximately 15 MPa at the point of failure (2500s). During the same period of time Young's modulus decreases from 10 to 8 GPa. As the isostatic stress state is re-achieved (3000s) these values further change to is 0.35, 14.5 GPa and 6 MPa respectively (Fig. 7A-C). Finally, Poisson's ratio decreases only slightly to 0.34 as the effective pressure increases stepwise from 5 to 30 MPa. However, the remaining parameters all increase linearly with

increasing effective pressure to 20 and 9.5 GPa for Bulk and Young's modulus respectively, except for the first step in each case (2500s – 3500s).

3.2. Fluid-flow data of SNGP samples

The pre-deformation fluid flow (permeability) of intact (i.e. unfractured) SNA was too low to be measured in our setup via the steady-state-flow method, suggesting that permeability is lower than approximately 10^{-20} m^2 or 10^{-4} μl/s, even for integrating flow volume over several days. During the post-failure stage of the SNGP experiments, a differential fluid pressure was applied to pair of fluid ports (Fig. 2) to generate fluid flow. For SNA samples, a flow-rate of 7.7 μl/s was initially measured at 5 MPa confining pressure, decreasing with each increase in effective pressure 0.3 μl/s at 30 MPa (Fig. 4). For SNV samples which have higher natural (background) porosity, the fluid flow was far higher. At 5 MPa immediately after sample fracture, a flow rate of 10.2 μl/s was measured, decreasing in steps with increasing effective pressure to 5 μl/s (Fig. 6). This compares to a background flow rate of 6.72 μl/s (equivalent to a permeability of 10^{-17} m^2 across a homogeneous cylinder of 4cm diameter) before deformation (unfractured sample) at 5 MPa effective pressure.

3.3 Acoustic Emission stimulation at high temperature

Select experiments using the low porosity samples were repeated at high temperature (175 ºC) using phase 2B of the protocol described earlier (Figure 3) at three confining pressure conditions (10 MPa, 20 MPa, and 50 MPa). At a confining pressure of 10 MPa, and an initial pore fluid venting pressure of 5 MPa, we record an increase in AE reaching 250 hits at the point of pressure release (Fig. 8). Here, the AE hit rate increases rapidly from zero to 250 counts/0.1 ms at 128.5s (the moment of fluid pressure release). The count-rate then briefly decreases only to increase again starting at 129s. During this time (128.5 – 129.5s) we note the pore pressure remains largely constant at 0.8 MPa. This is followed by a final increase in AE at 130-131s which coincides with the final decrease in pore pressure to ambient conditions. Throughout the venting process, axial strain remains at constant level suggesting minimal sample movement.

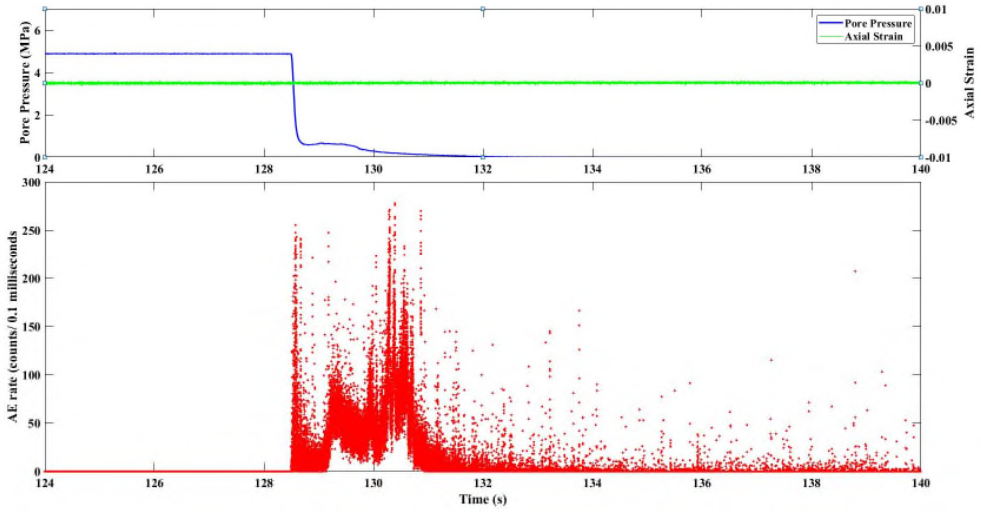

Figure 8. Spike in acoustic emission at the point of pore fluid decompression (~128.5s) for confining pressure of 10 MPa and pore fluid pressure of 5Ma.

Data for fluid venting at 20 MPa confining pressure and a pore fluid pressure of 10 MPa are shown in figure 9. At the onset of pore pressure release (141.5s), a swarm of AE is recorded reaching 100 counts/0.1 milliseconds before subsiding to between 20-50 counts/s, during which time the pore pressure remains at just under 1 MPa (141.5-142.5s). After this, an emergent increase in AE rate is recorded up to nearly 350 counts/0.1 milliseconds, accompanied by pore pressure reduction to zero (143s). Measurement of axial strain data does not show any movement, again suggesting that the fluid venting and the rock-fluid coupling solely generate the AE output during the pressure release, combined with the phase change of liquid water to a water/steam mixture, similar to the data and protocols reported in Benson et al. (2014) and Fazio et al. (2017).

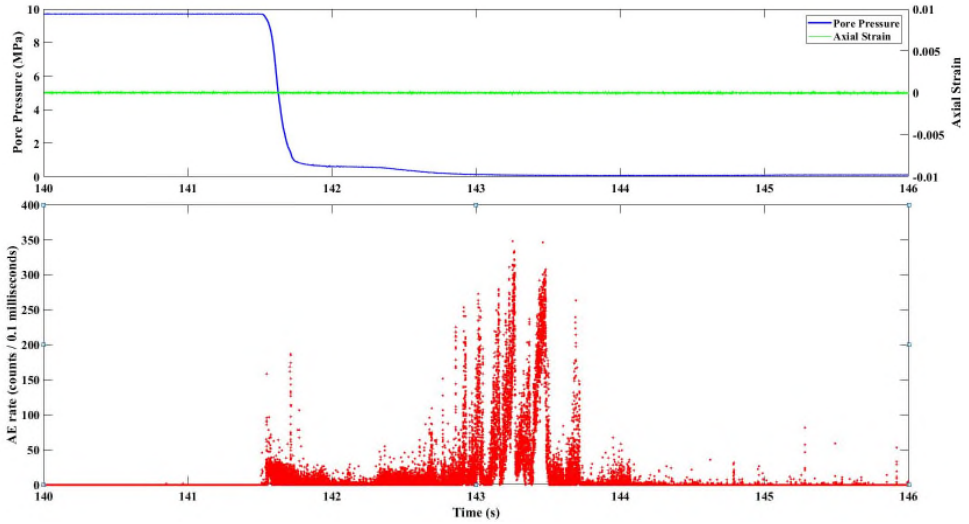

Figure 9. AE hits before and after pore fluid decompression at 10 MPa pore pressure and 175 °C temperature condition at 20 MPa coinciding with spikes in AE hits from approximately 141.5s.

At 50 MPa confining pressure and a pore pressure of 19.2 MPa, the rapid pore fluid venting at 93.8s coincides with AE count rate of approximately 450 counts/0.1 milliseconds (Figure 10) by 94.1s. The elevated AE hit rate persists from this point to the end of the recording at 98s, but with a clearly underlying decrease in the event rate when the 'spikes' in activity are considered. Pore pressure again remains elevated at approximately 0.8 MPa before decreasing to ambient pressure from approximately at 95 s. Although not as clear as previous data (Fig 8 and 9), the AE hit rate also decreases by this time, and remains at a background level of 20-50 counts/s from 95s, once the periodic 'spikes' in AE are neglected. As before, we note that axial strain remains constant after pore fluid decompression, similar with the other venting experiments, and indicating minimal to no movement in the deformed sample.

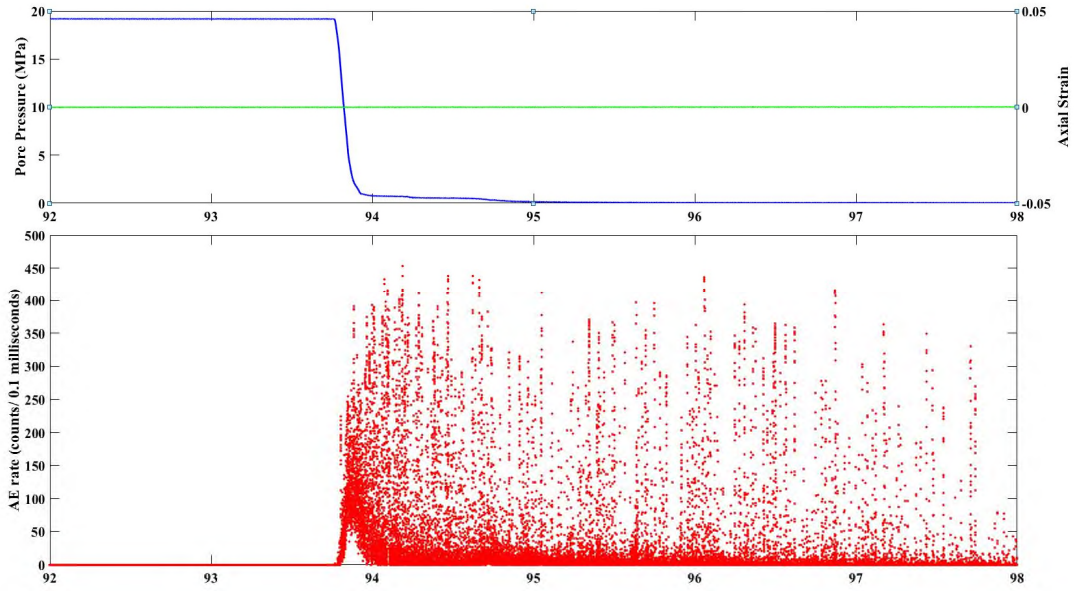

Figure 10. AE hits before and after pore fluid decompression at 19.2 MPa and 175 °C temperature condition and 50 MPa confining pressure. Pore fluid pressure briefly stays at 0.8 MPa after venting from 94 to 95 s.

4. Discussion and Conclusions

Seismic velocities are commonly utilized to infer the state of material as a response to changing pressure and temperature conditions (e.g. Nasseri et al., 2004; Benson et al., 2008). Development of secondary structures, both macro and micro, are known to significantly influence P and S-wave velocities and are thus useful in energy resources exploration (e.g. Nara et al., 2011; Vinciguerra et al., 2005). Experiments carried out on andesite and volcaniclastic rock samples highlight the sensitivity of the seismic properties to macro and micro-crack opening and closing as a result of progressing pressure conditions. At the early stage of deformation where crack closure and compaction is dominant, P and S-waves exhibit increasing trends that suggest sample stiffening. Conversely, crack propagation leading to failure and sample deformation is marked by large reduction in velocities in both andesite and the volcaniclastic rock.

Using elastic wave velocity data, dynamic material parameters are also calculated. This is useful, as these parameters are often more sensitive to environmental effects and fractures than elastic wave data alone. However, we do also note that dynamic elastic constants may differ to static constants as calculated using direct mechanical means (e.g. Heap et al., 2009). In general, however, the development of fracture due to applied stress decreases dynamic material

parameters, with the exception of Poisson's ratio which increases. The application of subsequent effective pressure increases both P-wave and S-wave velocities and elastic properties, again with the exception of Poisson's ratio. Of the three elastic properties, bulk modulus is particularly sensitive to damage formation. This is consistent with previous studies that examined dynamic moduli in different rock types subjected to high temperature and pressure conditions that result in the formation of both macro and micro fractures (e.g. Ayling et al., 1994; Heap et al., 2009; Blake and Faulkner, 2015).

The use of dynamic elastic parameters aside from the conventional velocity models are highlighted further on the seismic data gathered from SNGP. As shown in figure 11, seismic tomography results allowed examination and correlation of velocity models and other elastic parameters to subsurface data from a drilled well. Permeable zones are encountered below the production casing shoe (PCS) from 250 to 0 meters and from -300 to -500 meters elevation. These zones of high fluid flow coincide with relatively low Vs from 2 to 2.5 km/s and transitioning Poisson's ratio values from 0.15 to 0.3. The permeable zones are separated by an approximately 300 meters thick layer with a different seismic attribute, having relatively high Vs from 2.5 to 3 km/s and reduced Poisson's ratio of around 0.1. This horizon of absent permeability and increased S-wave velocity suggest that the encountered formation is competent and without fracturing. The thick zone of low Vs (around 1.5 km/s) and high Poisson's ratio (>0.3) above the PCS or within the closed-off section of the well likely represents the cap rock of the geothermal system consisting mainly of low permeability but highly porous clay minerals.

Permeability at depth in SNGP is reported to be controlled mainly by faults and fractures based on well data (Pastoriza, 2017). These fractured formation or zones of high fluid flow can be identified using velocities and elastic parameters which, under laboratory setting, exhibit reduction with fracture development (except Poisson's Ratio).

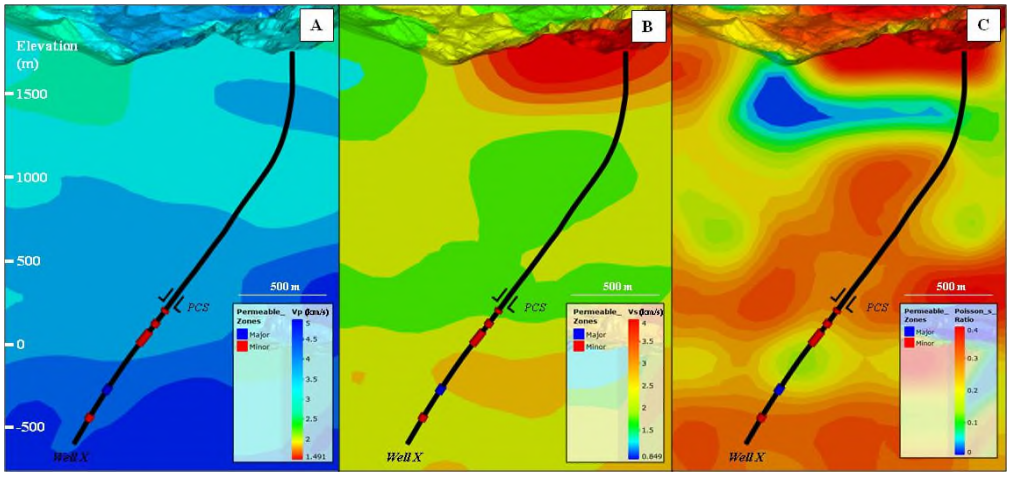

Figure 11. Vp (A), Vs (B) and Poisson's ratio (C) models derived from field seismic data in SNGP. Also shown is a drilled well in the area (Well X) with permeable zones encountered (red and blue line along the well track) and the production casing shoe (PCS) which marks the start of the open-hole section of the well.

Using the measured steady state flow across the generated shear damage zone, we have applied a set of fixed-thickness 'slots' (2-10mm) and the post-test length and width of the fracture, to calculate an effective permeability using equation (1). As shown in figure 12, SNA samples develop an effective permeability at 5 MPa ranging from 2.7×10^{-15} (10mm) to 2.7×10^{-14} m^2 (2mm), decreasing to between 6.0×10^{-16} to 6.0×10^{-17} m^2 at 30 MPa. For SNV, the fracture permeability ranges from 3.95×10^{-15} (10mm) to 3.95×10^{-14} m^2 (2mm) at 5 MPa to less than 1.0×10^{-15} m^2 (10mm) at 30 MPa confining pressure. The lower overall permeability (both in terms of effective permeability model and raw flow rate data) of SNA compared to SNV is clearly evident. In addition, SNA data show a faster rate of decrease at lower pressures (5 to 15 MPa). This is a common trend in freshly fractured rocks with low background permeability (e.g. Benson et al., 2006). With increasing pressure, the planar fractures are easily closed with application of confining pressure, resulting in significant reduction in fluid flow. In comparison, the higher porosity of the SNV sample has the effect of smoothing out the decrease in flow rate over the same period (5-15 MPa) whilst also providing an elevated background flow rate due to the more distributed nature of the flow which is not constrained to the damage zone. This is consistent with data from Seljadur Basalt (Nara et al., 2011) showing that while both macro-fractures and micro-cracks contribute heavily to permeability at low confining pressures, micro-cracks tend to dominate at higher confining pressures as macro-fractures are easily closed and restrict fluid movement.

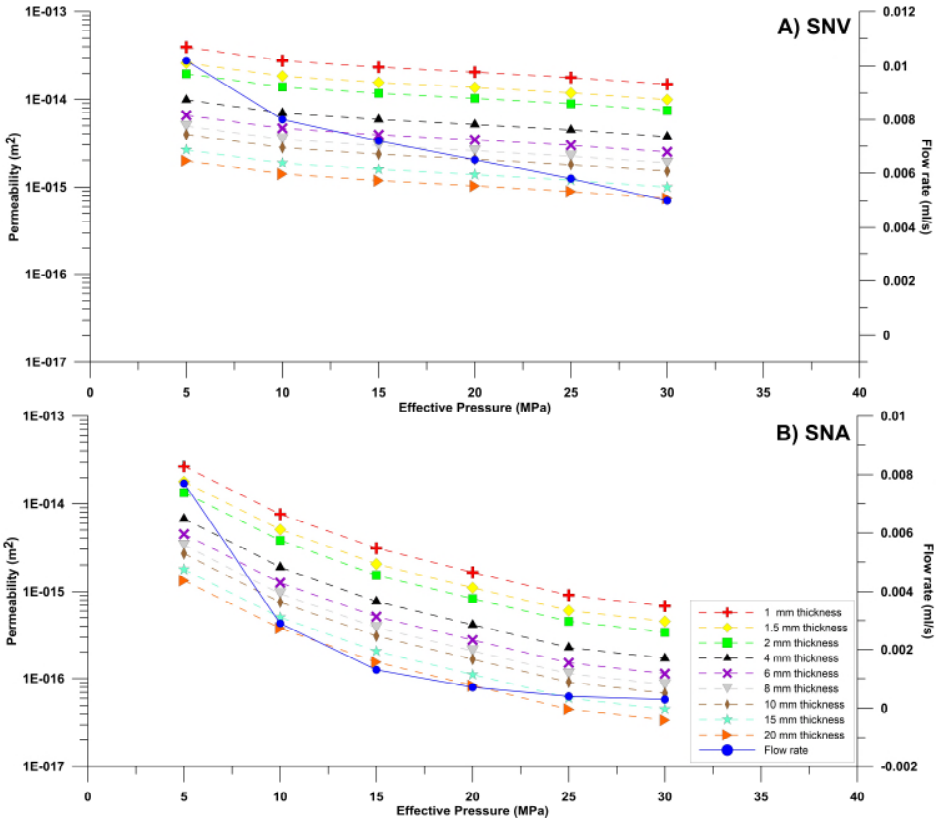

Figure 12. Effective permeability as a function of effective confining pressure after failure (fracture formation) in porous volcaniclastic rock of 12% (SNV, panel A) and non-porous andesite of 1% porosity (SNA, panel B)

We further note (Fig. 12) that a simple model of the changing fracture thickness does not match the change in the flow rate data. This suggests a more complex control on overall permeability (flow rate), such as crack and fracture closure and pore collapse (e.g. Benson et al., 2006; Baud et al., 2012). The exception is the SNA data at pressures higher than approximately 15MPa, which matches well to a fracture damage zone of 20mm thickness from pressures between 15-20 MPa, suggesting that for initially low porosity rock, the geometry of freshly generated damage zone is not altered significantly by application of pressure. Above 20MPa, the decreasing fracture thickness then exerts the key influence on the still-reducing fluid flow in the sample. Reversing this analysis, by setting a constant damage zone permeability of 10^{-15} m^2, illustrates the effect (Figure 13) with SNV showing a constant decrease in effective damage zone thickness from 10-15 MPa effective pressure whereas for SNA the decrease is very low. This is important, as high temperature geothermal systems are often found situated in tectonically active regions and in volcanic complexes, relying on faults for permeability and abnormally high geothermal gradients for heat flux. This, together with

515 resource development activities such as fluid extraction and injection, makes such systems
516 dynamic and prone to changes in a relatively short period of time, allowing a significant
517 secondary permeability to be stimulated. As highlighted in our data, changes in the rock
518 properties may be inferred from a variety of seismic attributes (Bulk and Young's modulus,
519 Poisson's ratio, and AE). We find that these are often more sensitive that elastic wave velocity
520 alone, revealing that high fracture permeability at low confining pressure coincides with
521 significant reduction in seismic attributes with the exception of Poisson's ratio. Conversely,
522 reduction in permeability by fracture closure and material stiffening results in a decrease in
523 Poisson's ratio but increase in bulk modulus and Young's modulus.
524

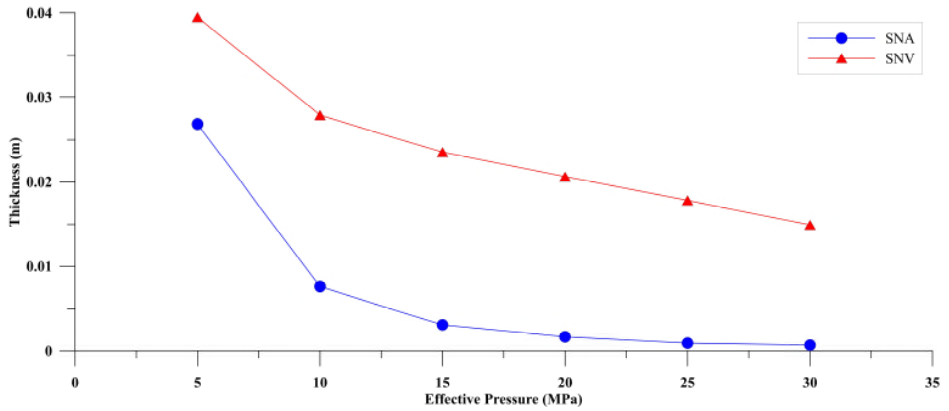

525
526 *Figure 13. Apparent fault zone thickness as a function of effective confining pressure after failure (fracture formation) for a*
527 *constant permeability of 1x10^{-15} m^2.*

528

529 Fluid flow is known to generate passive seismicity, and in many cases, this has been the
530 cause of significant geohazard (e.g. Giardini, 2009; Bachmann et al., 2012) especially if
531 unknown faults are present in the rock mass. To further develop this, we conducted a short
532 series of tests focussing on the fluid-rock interaction to induce seismic swarms at elevated
533 temperatures across a range of confining pressures at relevant geothermal conditions (Figures
534 8-10). During our simulations a prominent swarm in AE is generated at the moment of pore
535 pressure release with the AE broadly increasing with pore pressure. This is consistent with
536 similar experiments (e.g. Benson et al., 2008; Benson et al, 2015; Fazio et al., 2019) which have
537 linked fluid-rock interaction in fracture damage zones to swarms of AE activity due to fluid
538 turbulence. In addition, at high temperatures the transition of water into steam (during the
539 pressure release) has been linked to AE swarms at a lower characteristic frequency compared

to room temperature control experiments (e.g. Benson et al., 2015). This is seen in our experiments using the same protocol (Fazio et al., 2017) whereby pore pressure data in all experiments stabilises briefly at approximately 0.8 MPa during the swarm duration; this corresponds to the water to steam transition at 175 °C following the boiling point pressure curve, as used in the experiments and consistent with geothermal reservoir conditions using a two-phase fluid. This suggests that geothermal extraction at lower depths (>2 km) is more likely to generate seismicity and potential instability in the local rock mass, such as via the reactivation of critically stressed faults and fractures. Fault reactivation has been documented to occur not just by fluid pressure increase, but by steam as well (Romero et al., 1995).

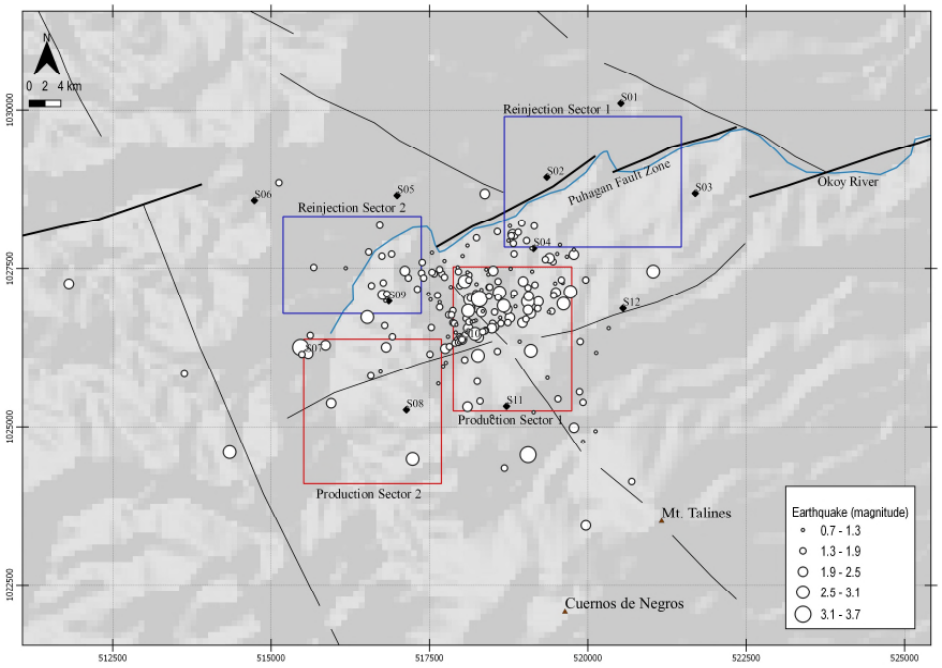

Figure 14. Recorded microearthquakes in SNGP after 6 months of data gathering (white circle). The production (red rectangle) and reinjection (blue rectangle) sectors are also shown.

Actual field data from SNGP highlights the effect of fluid extraction to seismicity. As shown in figure 14, most earthquake epicentres are found south of the Okoy River where the production sectors are situated. These earthquakes have magnitude values ranging from <1 to 3.7. Conversely, earthquake occurrences at the reinjection sectors were minimal. The contribution of injection activities to seismicity is well understood in geothermal fields, albeit

in Enhanced Geothermal Systems (e.g. Cuenot et al., 2008; Horalek et al., 2010). This is caused by pore fluid pressure increase, which reduces the effective normal stress that locks faults and fractures and drives these critically stressed structures to exceed its failure shear stress and promotes movement. Another mechanism from which earthquakes are generated is by hydraulic fracturing that creates tensile cracks when the minimum stress is exceeded. However, seismic data from a naturally permeable and convective geothermal system (SNGP) suggests that injection of fluids has minimal effect on overall seismicity, implying further that fluid injection pressure is below the needed pressure level to induce fault movement and generate fresh cracks. Production activities appear to have more impact on the seismicity of SNGP than fluid injection.

Monitoring of earthquakes in oil and gas fields reveals that production induced seismicity is associated with collapse and compaction of void spaces (Doglioni, 2018) and normal fault activation, triggered by extraction of fluids and reduction in failure criterion (e.g. Zoback and Zinke, 2002; Doglioni, 2018). This mechanism of normal faulting and compaction appears to occur in the production sector of SNGP as a response to long period of fluid extraction, reflected on the location alone of recorded microearthquakes. However, a significant difference is observed between the two production sectors, with sector 1 exhibiting very high seismicity than sector 2 (Figure 14). This is possibly explained by the difference in pressure conditions (Malate et al., 2008), subsurface lithology (Rae et al., 2004) and length of production history, with sector 1 producing a decade earlier. Haug et al., (2017) have shown that normal faulting as a response to fluid extraction can be influenced by several factors such as the character of the fault (dip and throw), thickness and depth of the reservoir where fluids are extracted and geomechanical properties of the surrounding rocks.

Seismicity in SNGP can be attributed to normal faulting and collapse mechanisms that generate earthquakes (Bromley et al., 1987; Sewell et al., 2015; Sherburn et al., 2015). However, based on the laboratory experiments conducted in this study, rapid fluid movement and phase change can also contribute to the seismicity of the field. Experiments carried out in the laboratory shows that AEs are generated with pore fluid venting without deformation in the sample. As shown in figures 8, 9 and 10, contraction along the axial length of the samples did not occur with the decompression of pore pressure, reflected on unchanged axial strain across

591 all the phase 2B experiments. This suggests that aside from fault movement and reservoir
592 compaction due to fluid extraction, the reported expansion of the two-phase zone (e.g. Malate
593 and Aqui, 2010) in the SNGP affects seismicity.
594
595 We conclude that P and S wave velocities and calculated elastic attributes such as Poisson's
596 ratio, bulk and Young's moduli are sensitive to pressure changes and can be used to infer the
597 state of material at depth (e.g. Blake and Faulkner, 2020). The formation of shear fractures that
598 weakens the material decreases the attributes while increasing pressure conditions that
599 strengthen the material via fracture closure increases the overall properties (Fig. 4, 6). We also
600 note that increasing depth of burial, simulated by increasing pressure conditions, consistently
601 reduces fluid flow. Given the protocol used for generating the samples, the pore space is likely
602 to comprise of both a background (or primary) porosity inherent to the material, as well as the
603 fracture damage zone generated due to the fault (secondary porosity). As shown in figure 13,
604 the sample with lower initial porosity (SNA) shows a faster apparent fracture thickness
605 reduction within the first few MPa of effective pressure, consistent with flow dominated by a
606 single larger structure (fracture). This is consistent with recent work suggesting that
607 permeability reduction due to increased pressure may show lesser effect on geothermal
608 reservoirs that rely on both primary and secondary structures (e.g. Cant et al., 2018). Finally,
609 we conclude that AE may be directly generated through fluid movement and phase change at
610 temperature conditions consistent with those found in geothermal reservoirs. The extraction of
611 large quantities of fluids under high temperature is likely to contribute to the overall seismicity
612 in a region, in addition to that generated from fracture development related to fluid injection
613 and fault movement. Although not the focus of this study, monitoring of geothermal reservoirs
614 with seismic sensors (AE in the laboratory) has the potential to resolve both the 4D source and
615 character of the event (e.g. source mechanism, frequency vs magnitude). Larger scale
616 implementation of this would therefore be of benefit in understanding associated geohazards in
617 high temperature geothermal fields.
618
619

5. References

Aurelio, M.A., Pena, R.E., Taguibao, K.J.L.: Sculpting the Philippine archipelago since the Cretaceous through rifting, oceanic spreading, subduction, obduction, collision and strike-slip faulting: Contribution to IGMA5000. Journal of Asian Earth Sciences, Vol. 72, (2013), 102 – 107, doi: 10.1016/j.jseaes.2012.10.007.

Ayling, M.R., Meredith, P.G., Murrell, S.A.F.: Microcracking during Triaxial deformation of porous rocks monitored by changes in rock physical properties, I. Elastic-wave Propagation Measurements on Dry Rocks. Tectonophysics, 245, (1995), 205-221, doi: 10.1016/0040-1951(94)00235-2.

Bachmann, C.E., Wiemer, S., Goertz-Allmann, B.P., Woessner, J.: Influence of pore-pressure on the event-size distribution of induced earthquakes. Geophysical Research Letters, 39, (2012), L09302, doi: 10.1029/2012GL051480.

Baud, P., Meredith, P., Townend, E.: Permeability evolution during triaxial compaction of an anisotropic porous sandstone. Journal of Geophysical Research, 117, (2012), B05203, doi: 10.1029/2012JB009176.

Benson, P. M., Meredith, P. G., & Schubnel, A. (2006). Role of void space geometry in permeability evolution in crustal rocks at elevated pressure. *Journal of Geophysical Research: Solid Earth*, *111*(12). https://doi.org/10.1029/2006JB004309

Benson P.M., Thompson, B.D., Meredith, P.G., Vinciguerra, S., Young, R.P.: Imaging slow failure in triaxially deformed Etna basalt using 3D acoustic-emission location and X-ray computed tomography. Geophysical Research Letters, 34, (2007), L03303, doi: 10.1029/2006GL028721.

Benson, P. M., Vinciguerra, S., Meredith, P.G., Young, R.P.: Laboratory simulation of volcano seismicity. Science, 322, (2008), 249–252, doi: 10.1126/science.1161927.

Benson, P. M., S. Vinciguerra, M.H., Nasseri, Young, R.P.: Laboratory simulations of fluid/gas induced micro-earthquakes: Application to volcano seismology. Frontiers in Earth Sciences, 2, (2014), 32, doi: 10.3389/feart.2014.00032

Birch F.: The velocity of compressional waves in rocks to 10 kilobars: 1. Journal of Geophysical Research, 65, (1960), 1083-1102, doi: 10.1029/JZ066i007p02199.

Blake, O.O., Faulkner, D.R.: The Effect of Fracture Density and Stress State on the Static and Dynamic Moduli of Westerly Granite. Journal of Geophysical Research: Solid Earth, 121, (2016), 2382-2399, doi: 10.1002/2015JB012310.

Blake, O.O., Faulkner, D.R.: Using Velocities, Density, and Bulk Modulus to Predict the Permeability Evolution of Microfractured Rocks. Rock Mechanics and Engineering. (2020), doi: 10.1007/s00603-020-02163-7

Bonner, B., Hutchings, L., Kasameyer, P.: A Strategy for Interpretation of Microearthquake Tomography Results in Salton Sea Geothermal Field Based upon Rock Physics Interpretations of State 2 14 Borehole Logs. Proceedings, Geothermal Resource Council Annual Meeting, San Diego, California (2006), doi: 10.5772/intechopen.81226

Bromley, C.J., Pearson, C.F., Rigor, D.M., PNOC-EDC.: Microearthquakes at the Puhagan Geothermal Field, Philippines – A case of induced seismicity. Journal of Volcanology and Geothermal Research, 31, (1987), 293-311.

Browning, J., Meredith, P., Gudmundsson, A.: Cooling-dominated cracking in thermally stressed volcanic rocks. Geophysical Research Letter, 43, (2016), 8417–8425, doi: 10.1002/2016GL070532

Cant, J.L., Siratovich, P.A., Cole, J.W., Villenueve, M.C., Kennedy, B.M.: Matrix permeability of reservoir rocks, Ngatamariki geothermal field, Taupo Volcanic Zone, New Zealand. Geothermal Energy, 6, 2 (2018), doi: 10.1186/s40517-017-0088-6.

Castagna, A., Ougier-Simonin, A., Benson, P. M., Browning, J., Walker, R. J., Fazio, M., Vinciguerra, S:. Thermal damage and pore pressure effects of the brittle-ductile transition in Comiso limestone. Journal of Geophysical Research: Solid Earth, 123, (2018), doi: 10.1029/2017JB015105.

Cuenot, N., Dorbath, C., Dorbath, L.: Analysis of the Microseismicity Induced by Fluid Injections at the EGS Site of Soultz-sous-Forets (Alsace, France): Implications for the Characterization of the Geothermal Reservoir Properties. Pure Applied Geophysics, 162, (2008), 797-828, doi 10.1007/s00024-008-0335-7.

De Siena L., Thomas, C., Waite, G., Moran, S., Klemme, S.: Attenuation and scattering tomography of the deep plumbing system of Mount St. Helens. Journal of Geophysical Research, 119, (2014a), 8223-8238, doi: 10.1002/2014JB011372

Doglioni, C.: A classification of induced seismicity. Geoscience Frontiers, (2018), 9, 1903-1909, doi: 10.1016/j.gsf.2017.11.015

Fazio, M., Benson, P.M., Vinciguerra, S.: On the generation mechanisms of fluid-driven seismic signals related to volcano-tectonics. Geophys. Res. Lett., 44, (2017), doi: 10.1002/2016GL070919

Fazio, M., Alparone, S., Benson, P. M., Cannata, A., & Vinciguerra, S. (2019). Genesis and mechanisms controlling tornillo seismo-volcanic events in volcanic areas. *Scientific Reports*, *9*(1). https://doi.org/10.1038/s41598-019-43842-y

Faulkner, D.R., Sanchez-Roa, C., Boulton, C., Den Hartog, S.A.M.: Pore Fluid Pressure Development in Compacting Fault Gouge in Theory, Experiments, and Nature, Journal of Geophysical Research: Solid Earth, 123, (2017), doi: 10.1002/2017JB015130.

Gehne, S., Benson, P. M.: Permeability and permeability anisotropy in Crab Orchard sandstone: Experimental insights into spatio-temporal effects. Tectonophysics, (2017) 712–713, 589–599, doi: 10.1016/j.tecto.2017.06.014.

Gehne, S., Benson, P. M., Koor, N., Dobson, K. J., Enfield, M., Barber, A.: Seismo-Mechanical Response of Anisotropic Rocks Under Hydraulic Fracture Conditions: New Experimental Insights. Journal of Geophysical Research: Solid Earth, 124(9), (2019), 9562–9579, doi: 10.1029/2019JB017342.

Geraud, Yves, et al.: Physical properties of fault zones within a granite body: example of the Soultz-sous-Forêts geothermal site. Comptes Rendus Geoscience, 342,7-8 (2010): 566-574.

Giardini, D.: Geothermal quake risks must be faced. Nature, (2009), 462, 848-849, doi: 10.1038/462848a.

Harnett, C.E., Benson, P.M., Rowley, P., Fazio, M.: Fracture and damage localization in volcanic edifice rocks from El Hierro, Stromboli and Tenerife. Nature Scientific Report, 8, (2018), 1942, doi: 10.1038/s41598-018-20442-w.

Haug, C., Nüchter, J.A., Henk, A.: Assessment of geological factors potentially affecting production-induced seismicity in North German gas fields, Geomechanics for Energy and the Environment, (2018), 16, 15-31, doi: 10.1016/j.gsf.2017.11.015.

Heap, M.J., Vinciguerra, S., Meredith, P.G.: The Evolution of Elastic Moduli with Increasing Crack Damage during Cyclic Stressing of a Basalt from Mt. Etna Volcano, Tectonophysics, 471, (2009), 153-160, doi: 10.1016/j.tecto.2008.10.004.

Hutchings, L., Bonner, B., Jarpe, S., Singh, A.: Micro-earthquake Analysis for Reservoir Properties at the Prati-32 Injection Test, The Geysers, California, Proceedings, Fortieth

741 Workshop on Geothermal Reservoir Engineering, Stanford University, Stanford, California
742 (2015), doi: 10.13140/2.1.2474.2404.
743
744 Hochstein, M.P.: "Classification and assessment of geothermal resources." In: Dickson MH and
745 Fanelli M (eds) Small geothermal resources, UNITAEWNDP Centre for Small Energy
746 Resources, Rome, Italy, (1990), 31-59.
747
748 Horálek, J., Jechumtálová, Z., Dorbath, L.: Source mechanisms of micro-earthquakes induced
749 in a fluid injection experiment at the HDR site Soultz-sous-Forêts (Alsace) in 2003 and their
750 temporal and spatial variations, *Geophys J Int*., (2010), 181(3), 1547- 1565, doi:
751 10.1111/j.1365-246X.2010.04506.x
752
753 Jarvis, A., Reuter, H.I., Nelson, A., Guevarra, E.: Hole-filled seamless SRTM data V4,
754 International Centre for Tropical Agriculture (CIAT), (2008), available from
755 http://srtm.csi.cgiar.org.
756
757 Julian, B.R., Foulger, G.R.: Improved Methods for Mapping Permeability and Heat Sources in
758 Geothermal Areas Using Microearthquake Data, Proceedings, Thirty-Fifth Workshop on
759 Geothermal Reservoir Engineering, Stanford University, Stanford, California (2010).
760
761 Julian, B.R., Foulger, G.R., Monastero, F.C., Bjornstad, S.: Imaging Hydraulic Fractures in a
762 Geothermal Reservoir, Geophysical Research Letters, 37, (2010), L07305.
763
764 Kushnir, A.RL., Heap, M.J., Patrick Baud, P.: Assessing the role of fractures on the
765 permeability of the Permo-Triassic sandstones at the Soultz-sous-Forêts (France) geothermal
766 site, *Geothermics,* 74, (2018), 181-189.
767
768 Lockner, D., Byerlee, J., Kuksenko, V., Ponomarev, A., Sidorin, A.: Quasi-static fault growth
769 and shear fracture energy in granite, Nature, 350, (1991), 39-42, doi: 10.1038/350039a0.
770
771 Malate, R.C.M., Aqui, A.R., Orizonte Jr., R.G.: Sustaining and Optimizing Steam Production
772 in the Southern Negros Geothermal Production Field, Philippines, Proceedings of the 8th Asian
773 Geothermal Symposium, December 9-10, 2008.
774
775 Malate, R.C.M., Aqui, A.R.: Steam Production from the Expanded Two-Phase Region in the
776 Southern Negros Geothermal Production Field, Philippines, Proceedings World Geothermal
777 Congress 2010, Bali, Indonesia.
778
779 McLaskey, G.C., Lockner, D.A.: Preslip and Cascade Processes Initiating Laboratory Stick
780 Slip, Journal of Geophysical Research: Solid Earth, 119, (2014), doi: 10.1002/2014JB011220.
781

Nara, Y., Meredith, P.G., Yoneda, T., Kaneko, K.: Influence of Macro-fractures and Micro-fractures on Permeability and Elastic Wave Velocities in Basalt at Elevated Pressure, Tectonophysics, 503, (2011), 52-59, doi: 10.1016/j.tecto.2010.09.027.

Nasseri, M.H.B., Schubnel, A., Young, R.P.: Coupled Evolutions of Fracture Toughness and Elastic Wave Velocities at High Crack Density in Thermally Treated Westerly Granite, International Journal of Rock Mechanics and Mining Sciences, 44, (2004), 601-616, doi: 10.1016/j.ijrmms.2006.09.008.

Passelègue, F.X., Schubnel, A., Nielsen, A., Bhat, H.S., Deldicque, D., Madariaga, R.: Dynamic Rupture Processes Inferred from Laboratory Microearthquakes, Journal of Geophysical Research: Solid Earth, 121, (2016), doi: 10.1002/2015JB012694.

Pastoriza, L.R.: The geological characterisation and permeability evaluation of fractures in the Southern Negros Geothermal Field, Negros Island, Philippines, Doctoral Thesis, (2017), Doctoral Thesis, University of Durham, United Kingdom.

Pastoriza, L.R., Holdsworth, R.E., McCaffrey, K.J., Dempsey, E.: Tectonic Evolution of the Southern Negros Geothermal Field and Implications for the Development of Fractured Geothermal Systems, Geofluids, (2018), doi: 10.1155/2018/6025038

Rae, A.J., Cooke, D.R., Phillips, D., Yeats, C., Ryan, C., Hermoso, D.: Spatial and Temporal Relationships between Hydrothermal Alteration Assemblages at the Palinpinon Geothermal Field, Philippines: Implications for Porphyry and Epithermal Ore Deposits, Society of Economic Geologists, Special Publication, 2003.

Rae, A.J., Cooke, D.R., Phillips, D., Zaide-Delfin, M.: The nature of magmatism at Palinpinon geothermal field, Negros Island, Philippines: implications for geothermal activity and regional tectonics, Journal of Volcanology and Geothermal Research, vol. 129, no. 4, (2004), 321–342.

Romero, Jr., A.E., McEvilly, T.V., Majer, E.L., Vasco, D.: Characterization of the geothermal system beneath the Northwest Geysers steam field, California, from seismicity and velocity patterns. Geothermics, 24, (1995), 471-487, doi: 10.1016/0375-6505(95)00003-9.

Sewell, S.M., Cumming, W., Bardsley, C.J., Winick, J., Quinao, J., Wallis, I.C., Sherburn,S., Bourguignon, S., Bannister, S.: Interpretation of microseismicity at the Rotokawa Geothermal Field, 2008–2015. In: Proceedings World Geothermal Congress 19-25 April 2015, Melbourne, Australia.

Sherburn, S., Bromley, C., Bannister, S., Sewell, S., Bourguignon, S.: New Zealand Geothermal Induced Seismicity: an overview. Proceedings World Geothermal Congress 2015, Melbourne, Australia

Siratovich, P. A., Heap, M.J., Villenueve, M.C., Cole, J.W., Reuschle, T.: Physical property relationship of the Rotokawa Andesite, a significant geothermal reservoir rock in the Taupo Volcanic Zone, New Zealand. Geothermal Energy, 2, (2014), doi: 10.1186/s40517-014-0010-4.

Siratovich, P. A., Heap, M.J., Villeneuve, M.C., Cole, J.W., Kennedy, B.M., Davidson, J., Reuschle, T.: Mechanical behaviour of the Rotokawa Andesites (New Zealand): Insight into permeability evolution and stress-induced behaviour in an actively utilised geothermal reservoir. Geothermics, 64, (2016), 163-179, doi: 10.1016/j.geothermics.2016.05.005.

Vinciguerra, S., Trovato, C., Meredith, P.G., Benson, P.M.: Relating seismic velocities, thermal cracking and permeability in Mt. Etna and Iceland basalts. International Journal of Rock Mechanics & Mining Sciences, 42, (2005), 900–910, doi: 10.1016/j.ijrmms.2005.05.022.

Zoback, M.D., Zinke, J.C.: Production-induced normal faulting in the valhall and ekofisk oil fields, Pure Appl Geophys (Pageoph), 159, (2002):403–420,

Zucca, J.J., Hutchings, L.J., Kasameyer, P.W.: Seismic Velocity and Attenuation Structure of the Geysers Geothermal Field, California. Geothermics, 23, (1994), 111-126, doi: 10.1016/0375-6505(94)90033-7.